

Interstellar medium simulations

D. Breitschwerdt^{1,*}, M.A. de Avillez^{1,2}, J. Feige³, and C. Dettbarn⁴

¹ Zentrum für Astronomie und Astrophysik, Technische Universität Berlin, Hardenbergstr. 36, D-10623 Berlin, Germany

² Department of Mathematics, University of Évora, R. Romão Ramalho 59, 7000 Évora, Portugal

³ University of Vienna, Faculty of Physics – Isotope Research, VERA Laboratory, Währingerstr. 17, 1090 Vienna, Austria

⁴ Astronomisches Recheninstitut, Zentrum für Astronomie Heidelberg, Mönchhofstr. 12-14, D-69120 Heidelberg, Germany

Received 2012 Apr 14, accepted 2012 Apr 16

Published online 2012 Jun 15

Key words galaxies: ISM – ISM: evolution – ISM: structure – supernova remnants – solar neighborhood

In this review we critically assess numerical simulations of the interstellar medium (ISM), and argue that 3D high resolution calculations are the most promising method to determine the structure of the interstellar gas and follow its evolution well into the nonlinear regime. Based on a Riemann solver adaptive mesh refinement code, we present a model, which fulfills the basic requirements of running it sufficiently long in order to erase memory effects of the initial conditions, set up a disk-halo fountain flow cycle, for converging solutions with increasing mesh refinement. We obtain the following results: (i) in a supernova driven ISM, high Reynolds number turbulence generates structures on all scales, (ii) the volume filling factor of the hot gas is substantially reduced due to the fountain flow, (iii) gas clouds are transient shock compressed layers, (iv) more than half of the gas mass resides in thermally unstable regimes, (v) O VI is distributed in patchy mixing layers, with the derived column densities being in agreement with FUSE and Copernicus observations, (vi) the electron density distribution up to distances of 8 kpc in the disk is consistent with pulsar dispersion measure observations, provided that the electron and ionization structure are not in equilibrium, (vii) the interstellar cooling function depends both on *space and time* (and not only on temperature and metallicity), (viii) the Local Bubble has been produced by 14–20 supernovae about 14 Myr ago, exploding in a moving group on its path through the local ISM, (ix) the nearest supernova explosion to Earth occurred 2.2×10^6 yr ago at a distance of ~ 85 pc, in agreement with measurements of the radionuclide ^{60}Fe found in the ferromanganese crust on the ocean floor.

© 2012 WILEY-VCH Verlag GmbH & Co. KGaA, Weinheim

1 Introduction

Galaxy evolution in general, and star formation in particular, is determined by the structure and evolution of the interstellar medium (ISM). Its discovery dates back more than 100 years ago by the observation of “stationary” Ca II lines in the spectrum of a spectroscopic binary star (Hartmann 1904), which were later found not to be of circumstellar origin. In addition, the extinction of star light pointed towards the medium between the stars to be filled with gas and dust. Before the launch of the UV satellite Copernicus in 1972, the ISM was thought to be composed of a cold and weakly ionized warm gas, which was adequately described by the so-called 2-phase model of the ISM by Field, Goldsmith & Habing (1969), in which low energy cosmic rays were the energy input, and line cooling the energy loss sources. The two stable phases were the result of thermal instability (Field 1965) acting on the gas when perturbed in entropy. The Copernicus observations gave birth to the so-called hot phase, by the detection of the widespread O VI absorption line (Jenkins & Meloy 1974), which was generated by supernova (SN) explosions, first theoretically described by a tunnel network of hot gas (Cox & Smith 1974),

and later by the so-called 3-phase model (McKee & Ostriker 1977, henceforth MO77). In their detailed account of energy balancing, the ISM was supposed to consist of clouds, which were time and again overrun by supernova remnant (SNR) shock waves, thus evaporating clouds, with its gas subsequently cool down. Apart from a molecular medium (MM), which is gravitationally bound, the remaining stable phases are the cold neutral (CNM), warm neutral (WNM) and warm ionized (WIM) medium, supplemented by a hot intercloud medium (HIM) cooling down. The three stable phases were assumed to be in pressure equilibrium and regulated by SNe with the surprising result that the HIM would have a volume filling factor of $f_{V,HIM} \sim 0.7$ or even higher. Thus the ISM would appear as a hot tenuous HIM plasma, interspersed by clouds with dense cores, which, like in an onion shell model, would represent the CNM, WNM and WIM (from inside out).

Just a few years earlier, using sounding rockets, Bowyer et al. (1968) have discovered the existence of a diffuse soft X-ray background (SXRb). Its spectral signature, however, was not consistent with the HIM, as it contained lines, requiring higher excitation temperatures, if the plasma was assumed to be in collisional ionization equilibrium (CIE). Shapiro & Field (1976) drew the compelling conclusion

* Corresponding author: breitschwerdt@astro.physik.tu-berlin.de

that the inconsistency of these observations must lead to the existence of an overpressure in the galactic disk, which would inevitably drive the plasma out into the halo, where it could cool and rain down on the disk in a so-called galactic fountain. The very soft emission in the 0.1–0.3 keV band must be very local due to the energy dependent photoelectric absorption cross section, $\sigma(E) \propto E^{-3}$, and a resulting small mean free path of soft X-ray photons, $\lambda_{\text{mfp}} \propto 1/(n\sigma) \sim 100$ pc, for an average ISM density of 1 cm^{-3} (McCammon & Sanders 1990). The local electron density $n_e \sim 5 \times 10^{-3} \text{ cm}^{-3}$ is found from absorption studies towards nearby clouds (e.g. Snowden et al. 1991) with known column density by fitting the foreground emission measure in the soft band; moreover, UV absorption measurements towards background stars, using e.g. Na I as a sensitive tracer for H I, show that a region of a similar size (or somewhat larger) is devoid of H I. This negative correlation between soft X-rays and neutral gas was generally interpreted by the Local (Hot) Bubble (LB), which, as will be shown in this paper, is a superbubble (SB), due to the spatial and temporal correlation of SN explosions.

Since about at least half of all SNe occur in associations, SBs are common features in the ISM. This was the basis of the so-called chimney model (Norman & Ikeuchi 1989), in which, according to the amount of hot gas generated, the upward flow into the halo either leaves the galaxy as a wind or is cycled back as a fountain, with the broken up shell of the SB resembling a chimney. The obvious consequence in both cases is the reduction of the HIM volume filling factor, in agreement with observations of H I holes in external galaxies.

All these models describe certain observational aspects of the ISM; however, a deeper understanding of the nonlinear evolution and structure of the ISM can only be achieved by numerical solutions of the full hydrodynamical (HD) or magnetohydrodynamical (MHD) equations. Early 2D global simulations on a $2 \text{ kpc} \times \pm 15 \text{ kpc}$ grid, which included star formation (SF), SNe, stellar winds and an optically thin cooling function (Rosen & Bregman 1995), showed that a multiphase medium is the result of the nonlinear evolution, and that the ISM structure depends on the SF rate. Unlike in the MO77 model, clouds do not appear to be spherical with the distribution of phases depending on the optical depth, but seem to be filamentary and easy to fragment. Wada & Norman (2001) included gravitational instability in their simulations, and could show that the probability density function (pdf) over a temperature range from 10^2 – $10^6 M_{\odot} \text{ pc}^{-2} \text{ K}$ is lognormal. Clearly turbulence, which is a natural consequence of the Navier-Stokes equations, has a profound influence on the structure of the ISM (see Elmegreen and Scalo 2004), as it couples flows on all scales. Since its character depends on the dimensionality of the flow, 3D simulations were necessary. The simulations of Korpi et al. (1999) also include the dynamo effect (see also Gressel et al. 2008), but their simulations box with 500×500 horizontal and 2 kpc vertical size is too small to capture

the full fountain flow, and follow the evolution for a sufficiently long time in order to erase memory effects of the initial conditions (see de Avillez & Breitschwerdt 2005). In Sect. 2, we describe a 3D high resolution ISM model (HD and MHD), in Sect. 3, simulation results are presented and discussed, and in Sect. 4 the LB as our closest patch of ISM is described; Sect. 5 closes with our conclusions.

2 3D high resolution simulations of the ISM

A realistic ISM simulation should include all important processes of heating and cooling, and treat the effect of SF in the dense regions of the disk. It has been shown (MacLow & Klessen 2004) that SN explosions are the main driver of the turbulent ISM. Owing to a rapid increase in computing power and the development and improvement of algorithms to solve hyperbolic partial differential equations on a grid with adaptive mesh refinement, it was possible to simulate representative parts of the ISM with high resolution in 3D. A complete simulation of a whole galaxy with sufficient resolution has still not been achieved, but is within the grasp of the near future. A fair compromise seem to be *mesoscale* ISM simulations, for which we use a 3D HD and MHD adaptive mesh refinement Eulerian code, based on de Avillez (2000) of the SN driven ISM in a region of the Galaxy centered at the Solar circle (de Avillez & Breitschwerdt 2004, 2005, henceforth AB04, AB05, respectively). The simulation box has a square disk area of 1 kpc^2 , extending to $\pm 10 \text{ kpc}$ (and recently up to $\pm 15 \text{ kpc}$) on either side of the Galactic midplane. These simulations capture both the large scale disk-halo-disk circulation and the small scale turbulence driven structures in the Galactic disk. Over the years, methods based on smoothed particle hydrodynamics (SPH) have become increasingly popular, mainly because they are relatively cost-saving, and some effort has been put into showing that their performance is equivalent to grid methods (e.g. Price & Federrath 2010). While in dense regions with sufficient mass, particle methods can provide adequate or even higher resolution than grid methods, diffuse low density regions like the HIM are badly represented. Therefore, the multiphase structure of the ISM and their transitions can best be modeled with grid based methods. The finest adaptive mesh refinement (AMR) linear resolution per kpc^3 box around the Galactic midplane comprised 1.25 pc, 0.625 pc and 0.5 pc, corresponding, respectively to effective grids of 800^3 , 1600^3 and 2000^3 cells. The latter resolution and effective grid has been used in the recent developments of the model since 2007.

The number and masses of stars, which have formed, are determined by an initial mass function (IMF) within a mass range of 8 and $60 M_{\odot}$, respectively. Lower mass stars also form, but are taken out of the simulations, because the background gravitational potential by the total stellar population is used. High mass stars evolve according to their masses, blowing a stellar wind into the surrounding ISM and finally explode as SNe II, Ib, and Ic (Cappellaro et

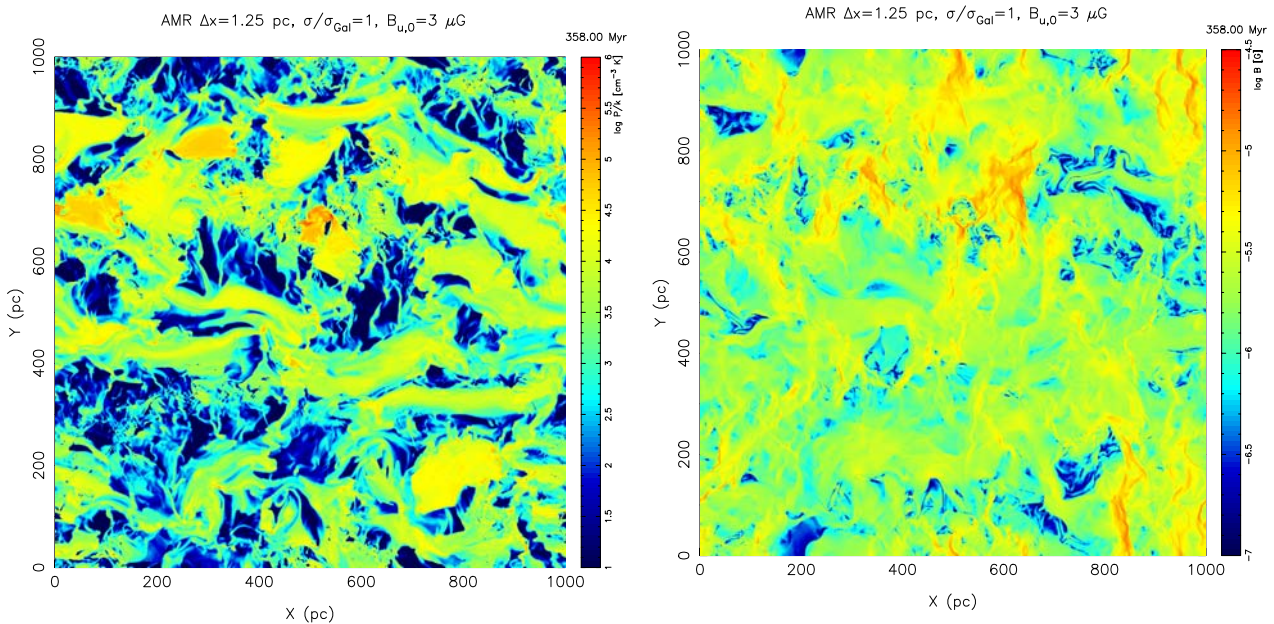


Fig. 1 Slices through the 3D data cube showing midplane pressure (*left panel*) and magnetic field, B , (*right panel*) distributions of MHD simulations (resolution 1.25 pc) at time $t = 358$ Myr. The colour coding is red (blue) for high (low) temperatures and B -field strengths, respectively. The initial regular disk parallel B -field is $3\mu\text{G}$; Fig. taken from AB05, reproduced with permission ©ESO.

al. 1999). SNe Ia explode randomly in an exponential disk having a scale height of 325 pc (Freeman 1987). SF is set up in a self-consistent way, but with the condition that the Galactic SN rate is met on average, and 60% of the explosions take place in clusters, the rest occurs randomly in the field. Regions with $T \leq 100$ K, $n > 10 \text{ cm}^{-3}$, forming under local self-gravity in converging flows with $\nabla \cdot \mathbf{v} < 0$ (\mathbf{v} being the gas velocity), are the sites of SF; for further details see AB04, AB05. The initial conditions start off from a vertical density distribution including molecular, neutral, ionized and hot gas phases (see e.g., Ferrière 2001). The boundary conditions are periodic along the vertical boundaries and outflow at the top and bottom faces of the grid. After 400 Myr of simulation a maximum of about 15% of the initial mass, or $\sim 0.25 M_{\odot} \text{ yr}^{-1}$ (for a total Galactic gas mass of $\sim 10^{10} M_{\odot}$ and a SF disk of 10 kpc radius), has been lost as a galactic wind. This corresponds to about 25% (17–41%) of the Galactic SF rate, which is $0.68\text{--}1.45 M_{\odot} \text{ yr}^{-1}$, derived from the Spitzer/IRAC GLIMPSE survey (Robitaille & Whitney 2010). This is definitely a non-negligible value, considering the fact, that predominantly chemically enriched material will be blown away.

3 Results

In the following subsection, the major results and implications of the ISM simulations will be presented and discussed. It will become evident that a 3-phase ISM in pressure equilibrium (the basic principle in the MO77 model), where cloud evaporation rate is balanced by dense shell formation rate and SN energy injection rate by radiative loss rate is not viable. Instead, over a wide range of tempera-

tures ($10^2 < T < 10^6$ K, AB05) the gas is dominated by ram pressure, and a large amount of energy is stored in turbulence, which alters the structure of the ISM significantly. For example clouds appear as shock compressed layers, and turbulent mixing is dominating heat conduction. Figure 1 shows that the magnetic field (right panel) is filamentary and disordered, and that the pressure distribution (left panel) spans more than 4 orders of magnitude, far from equilibrium; this can also be studied by the pressure pdfs (see AB05).

3.1 The role of turbulence

Observations of the ISM show a frothy and filamentary medium with structures on all scales (see e.g. the beautiful mosaic of the LMC, extracted from Spitzer SAGE IRAC/MIPS data, Meixner et al. 2006). Such an appearance is a natural consequence of a turbulent ISM, as has been proposed more than 60 years ago by von Weizsäcker (1951). This is not surprising considering the high Reynolds numbers in the ISM of about $10^5\text{--}10^7$ (Elmegreen & Scalo 2004). Supersonic turbulence constantly requires a high energy input rate. The ISM offers a variety of processes, ranging from large scale instabilities (hydrodynamic, gravitational, magneto-rotational) to small scale thermal (Field 1965) and cosmic ray driven streaming instability (Kulsrud & Pearce 1969), with SNe being the dominant energy input sources (see Sect. 2). Turbulence arises due to the nonlinear term $\mathbf{u}\nabla\mathbf{u}$ in the Navier-Stokes Equation (NSE). Still to this date there has been no proof of the existence of smooth and global solutions, which is one of the seven Millennium Prize Problems of the Clay Mathematics Institute. Apart from a

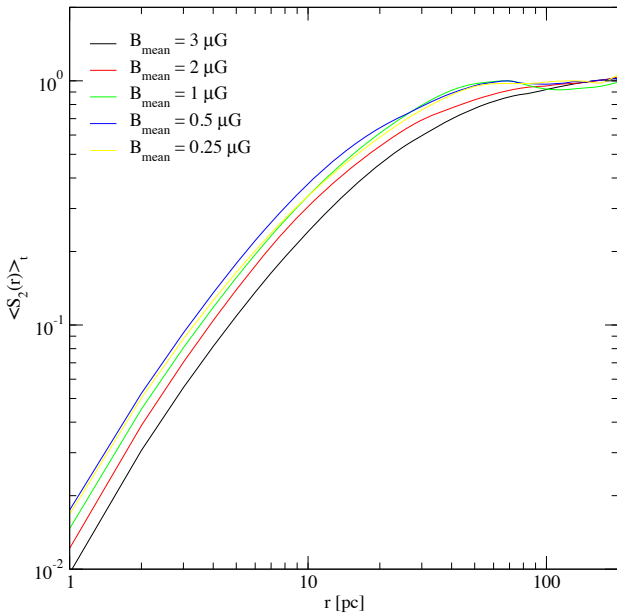


Fig. 2 (online colour at: www.an-journal.org) Second order structure function of an ISM simulation as a function of correlation length r . The correlation breaks down at scale length $l \sim 75$ pc.

statistical treatment using ensemble averages of the flow variables, scaling relations (e.g. Kolmogorov 1941, K41) give some insight into the nature of turbulence. Also numerical solutions are confronted with huge difficulties. In contrast to chaos theory, turbulent systems have a large number of degrees of freedom, and exhibit properties like intermittence. Even the most powerful computers can only calculate mildly turbulent flows with Reynolds numbers Re of the order of a few thousand in Direct Numerical Simulations (DNS), or neglect the small scales in Large Eddy Simulations (LES), bridging the gap with subgrid models.

Some insight into the physical nature of turbulence can be gained by reformulating the NSE (for incompressible flow) in terms of the vorticity $\boldsymbol{\omega} = \nabla \times \mathbf{u}$, which is a measure of the local angular rate of rotation of a fluid element,

$$\frac{D\boldsymbol{\omega}}{Dt} \equiv \frac{\partial \boldsymbol{\omega}}{\partial t} + (\mathbf{u} \cdot \nabla)\mathbf{u} = (\boldsymbol{\omega} \cdot \nabla)\mathbf{u} + \nu \Delta \boldsymbol{\omega}, \quad (1)$$

with ν being the kinematic viscosity of the flow. The first term on the RHS describes the change of the moment of inertia by stretching a fluid element, and the second the torque due to viscous stresses, i.e. spinning up or slowing down a fluid element. In summary, vorticity increases due to advection and diffusion, and the fluid can be pictured as a medium permeated by a large number of thin vortex tubes, which become longer and thinner and fill the whole space as long as the energy input on the largest (integral) scale is maintained. This illustrates the enhanced mixing rate in a turbulent fluid, where the turbulent viscosity is given by $\nu_t \sim Re \nu$.

The K41 scaling laws can be generalized for compressible flows under the assumption of scale-invariant density fluctuations (clouds) in the absence of magnetic fields and self-gravity. In a hierarchy of scales l , two successive levels

are given by $\rho_i/\rho_{i-1} = (l_i/l_{i-1})^{-D\alpha}$, where $0 \leq \alpha \leq 1$ and D are the compressibility and dimension of the flow, respectively. If α is independent of scale (and also of Mach number), it can be argued that the energy rate per unit volume $\rho u^3/l = \text{const}$ during the cascade, yielding a spectral energy density scaling law with respect to wavenumber $k = 2\pi/l$ of $E(k) \sim k^{-5/3-2\alpha}$ (Fleck 1996), for $D = 3$, which recovers the K41 law for incompressible flow ($\alpha = 0$). In other words, K41 scaling ($v \sim l^{1/3}$) can be restored by considering the density weighted velocity $v \equiv \rho^{1/3}u$ (Kritsuk et al. 2007, who give $\alpha = 0.15$ for forced isothermal turbulence). Deviations from K41 scaling is expected for higher order structure functions, since intermittency becomes more conspicuous. The structure function of order p can be defined by $S_p(l) := \langle |\mathbf{v}(\mathbf{r} + l\mathbf{e}_r) - \mathbf{v}(\mathbf{r})|^p \rangle \sim l^{p/3}$, since $v^p = \rho^{p/3}u^p \sim l^{p/3}$.

At which scale is turbulence fed into the system? If we want to study the correlation of the energy contained in turbulent eddies of size l , we look at the second order structure function, since $\langle (\Delta v(\mathbf{r}))^2 \rangle$ is proportional to the kinetic energy per unit mass. The largest size over which a correlation still exists is given by the flattening of $S_2(l)$. Our simulations show (s. Fig. 2) that this occurs at $l \approx 75$ pc (de Avillez & Breitschwerdt 2007), and is the average size of superbubbles (SBs) breaking up due to density inhomogeneities in the ISM.

3.2 The non-equilibrium ionization ISM structure

Soon after the discovery of the hot phase of the ISM, it was realized that, since cooling covers a temperature range of more than five orders of magnitude, the assumption of ionization equilibrium had to be put into question. Kafatos (1973) and Shapiro & Moore (1976) showed that an optically thin hot plasma will be driven out of equilibrium due to the inherent atomic differences in ionization and recombination rates. Hence, a plasma, which is initially in collisional ionization equilibrium (CIE) and cooling down from 10^6 K, will appear “overionized”, because recombination is lagging behind. Conversely, if a cold plasma is overrun by a shock wave, the kinetic electron temperature will increase steeply, and the ionization structure cannot follow, so that the plasma will look “underionized” (e.g. Cox & Anderson 1982). Breitschwerdt & Schmutzler (1994) have shown, that if a hot plasma undergoes fast adiabatic expansion, soft X-ray spectra will be dominated by the effect of delayed recombination, with emission in the 0.3–0.5 keV range at plasma temperatures of only $\sim 4 \times 10^4$ K. The resulting cooling function will be lower than in CIE, because much of the radiative energy is still stored in high ionization stages. Clearly, these time-dependent processes should have noticeable effects on the energy budget of the ISM. Since the cooling function is now also a function of space and time, viz., $\Lambda(T, Z; \mathbf{x}, t)$, the time-dependent ionization structure needs to be calculated simultaneously with HD/MHD evolution of the plasma; Z denotes the metallicity. We have recently solved this problem (de Avillez &

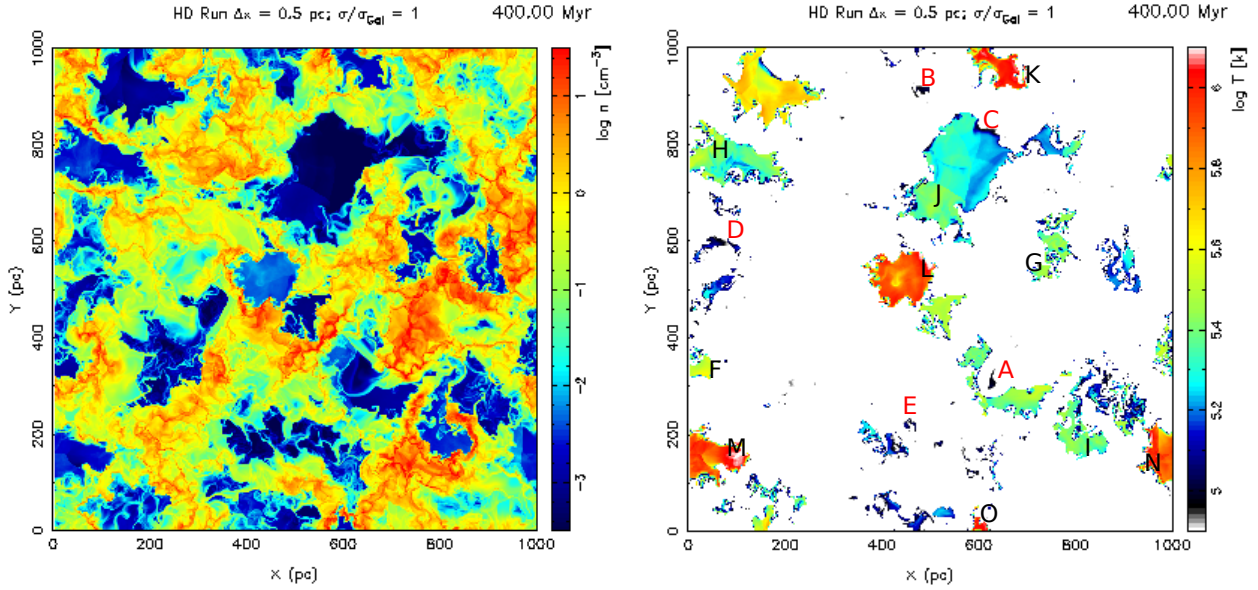


Fig. 3 Cut through the Galactic midplane of the non-equilibrium ionization density (*left panel*) and temperature filtered ($10^{4.9}$ – $10^{6.1}$ K; *right panel*) logarithmic distributions at 400 Myr (spatial resolution is 0.5 pc). Note that the change of colour coding: cold (high density) gas is shown in red, and hot (low density) gas in blue.

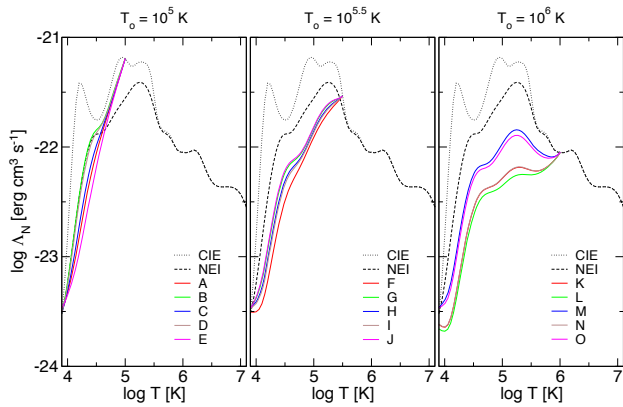


Fig. 4 Normalized NEI cooling functions at different locations in the Galactic midplane, corresponding to the labels in Fig. 3 (right panel) with initial temperatures of 10^5 K (labels A–E), $10^{5.5}$ K (labels F–J), and 10^6 K (labels K–O), respectively. The black dotted and dashed lines represent the CIE and NEI cooling, respectively. The latter was calculated for isochoric cooling of a completely ionized plasma at 10^9 K.

Breitschwerdt 2012a (AB12a), 2012b), by developing the E(A+M)PEC code, which presently includes electron impact ionization, inner-shell excitation autoionization, radiative and dielectronic recombination, charge-exchange reactions, continuum (bremsstrahlung and two-photon), free-bound and line (permitted, semi-forbidden as well as forbidden) emission in the range 1 \AA – $610\ \mu$ and molecular lines (for details see AB12a).

Figure 3 shows the NEI density structure (*left panel*) of the ISM in the Galactic midplane, and in the *right panel* a temperature filter of $10^5 < T < 10^6$ K has been applied, with specific regions being labeled in order to track their

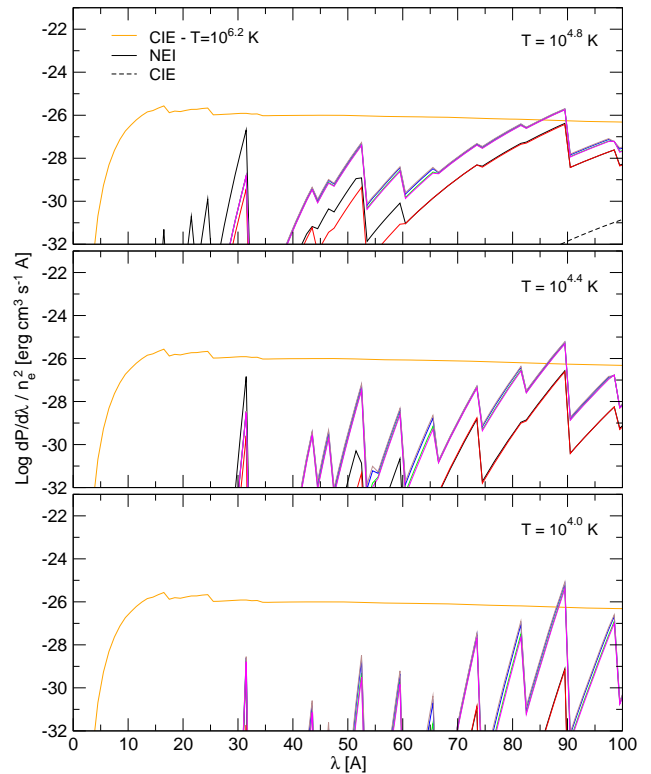


Fig. 5 Saw-tooth shaped recombination (free-bound) emission curves of the cooling gas located at sites F–J (right panel of Figure 3) with an initial temperature of $10^{5.5}$ K (cf. the corresponding cooling curves in Fig. 4). Solid and dashed black lines represent the free-bound emission expected from NEI and CIE static (i.e., no dynamics) plasma at the temperatures indicated. For comparison, a CIE plasma at $10^{6.2}$ K (orange curve) is shown.

evolution. Each of them has a different NEI history, and hence a spatially and temporally different cooling function, with significantly differing cooling rates (s. Fig. 4). The upper dashed line represents the CIE, and the dotted line below the static NEI density normalized cooling function, respectively, for reference. In the latter case, a fully ionized gas is assumed to cool down isochorically. If a plasma undergoes shock heating or fast adiabatic expansion, the kinetic electron temperature is increased or decreased dramatically, as the establishment of Maxwellians of electrons and subsequently of ions by collisions is generally much faster than attaining ionization equilibrium. Thus, for a gas cooling down, the middle and right panels of Fig. 4 show cooling functions below their static counterparts. If the temperature drops further, e.g. to 10^5 K, most of the highly ionized species in CIE have already recombined, whereas in the NEI case, recombinations are still ongoing, thus enhancing the cooling rate in this case. At higher temperatures (e.g. 10^6 K) the dynamic NEI cooling rate can be lower by more than one order of magnitude (s. Fig. 4, right panel).

It is also very instructive to have a look at the corresponding spectra, especially at low temperatures (s. Fig. 5). For comparison of the absolute emission rates, we have plotted a hot plasma ($10^{6.2}$ K) CIE spectrum with the same solar abundances, as in all the simulations. Due to the effect of *delayed recombination* we obtain soft X-ray spectra at temperatures as low as 2.5×10^4 K. Please note the dashed line in the lower right corner of the upper panel in Fig. 5, which gives the CIE spectrum at the corresponding temperature, i.e. at $10^{4.8}$ K. It goes without saying, that such an effect will have profound implications for the interpretation of soft X-ray and EUV spectra. At first glance, it seems to be a drawback compared to CIE, that now we are not able any more to infer a certain temperature of the ISM plasma according to the most abundant ionization stage. In CIE, the ionization fraction is strongly temperature dependent, so that e.g. the preponderance of OVI corresponds to $T \sim 3 \times 10^5$ K. In NEI, in contrast, the ionization fraction can be the same over a temperature range of two orders of magnitude (Breitschwerdt and Schmutzler, 1999). However, given sufficient spectral resolution, an observed spectrum is a fingerprint of the plasma's thermodynamic history, i.e. the existence of certain ionization stages, and their abundances, require a certain dynamical and thermal coupling, and may thus reveal some kind of *plasma archaeology*. In particular, different ionization stages of the same ion, e.g. oxygen, will give an abundance independent record of plasma evolution. We are currently investigating these issues in more detail.

3.3 Volume filling factors

A notable prediction of the MO77 model was the high volume filling factor (VFF) of 70–80 % of the HIM, which was based on the large average size of SN remnants (SNRs) in the disk and the evaporation of clouds by heat conduction. However, the spatial and temporal correlation of SNe gives

Table 1 Summary of the average values of volume filling factors and mass fractions of the disk gas at the different thermal regimes for the HD and MHD runs. Values are taken from AB05.

T [K]	$\langle f_v \rangle^a$ [%]		$\langle f_M \rangle^b$ [%]	
	HD	MHD	HD	MHD
<200 K	5	6	44.2	39.9
200– $10^{3.9}$	46	29	49.0	43.7
$10^{3.9}$ – $10^{4.2}$	10	11	4.4	8.5
$10^{4.2}$ – $10^{5.5}$	22	33	2.0	7.4
$>10^{5.5}$	17	21	0.3	0.5

^a Occupation fraction; ^b mass fraction.

Table 2 Dependence of the average volume filling factors of ISM phases for different SN rates. We averaged over 101 snapshots (of 1.25 pc resolution runs) between 300 and 400 Myr of evolution with time intervals of 1 Myr (Table from AB04).

σ^a	$\langle f_{v,cold} \rangle^b$	$\langle f_{v,cool} \rangle^c$	$\langle f_{v,warm} \rangle^d$	$\langle f_{v,hot} \rangle^e$
1	0.171	0.354	0.298	0.178
2	0.108	0.342	0.328	0.223
4	0.044	0.302	0.381	0.275
8	0.005	0.115	0.526	0.354
16	0.000	0.015	0.549	0.436

^a SN rate in units of the Galactic SN rate; ^b $T < 10^3$ K;

^c $10^3 < T \leq 10^4$ K; ^d $10^4 < T \leq 10^{5.5}$ K; ^e $T > 10^{5.5}$ K.

rise to a large overpressure in the disk and hence to a fountain and wind outflow (cf. the “chimney” model by Norman & Ikeuchi 1989). Table 1 shows that the VFFs are way below these values, e.g. 17 % and 21 % for Galactic SN rates for hot magnetized and unmagnetized ISM plasmas, respectively (see AB05). In a previous study (AB 2004) we have analyzed the dependence of the VFFs on the SN rate (s. Table 2). In sharp contrast to MO77, the VFF of the HIM is still less than 50%, even if the SN rate σ is 16 times the Galactic rate. Instead the warm phase ($10^4 < T < 10^{5.5}$ K), which corresponds to a thermally unstable regime(!) is dominating, again in stark contrast to the models of classical thermal stability (see Sect. 3.4). For the Galactic SN rate the VFF is dominated by the “cool” regime between 10^3 and 10^4 K, again comprising thermally unstable regimes.

3.4 Stability of gas phases

Observations of the WNM have revealed that contrary to the prediction of the 3-phase ISM model, 44 % of the gas are in the unstable temperature regime $500 < T < 5000$ K (Heiles & Troland 2003). Our simulations give a similar value of 55 % in this temperature range. To examine the distribution of gas in thermally unstable phases in more detail, we have plotted its distribution in a midplane cut (s. Fig. 6) in the classically unstable temperature regime $631 < T < 1585$ K. The distribution is very patchy and preferentially on small scales. All this can be understood, if we recall that the classical thermal stability analysis (Field

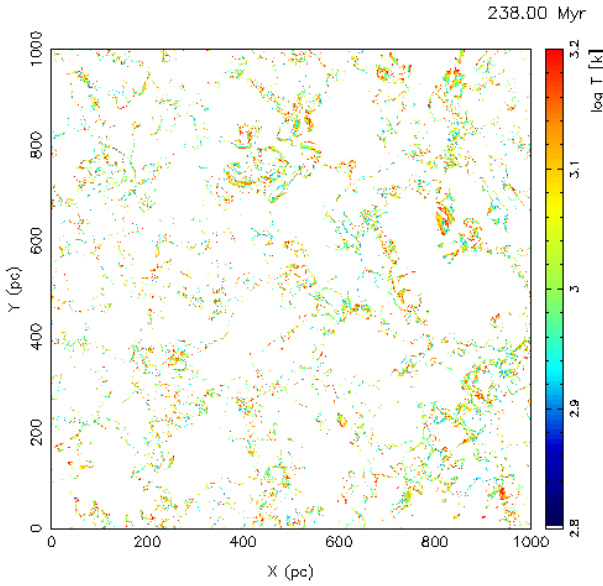


Fig. 6 2D snapshot of the Galactic plane taken from a HD run (resolution $\Delta x = 0.625$ pc) at time 238 Myr; note the filamentary structure of the warm neutral gas within the narrow temperature range $2.8 \leq \log(T) \leq 3.2$ K in the classically thermally unstable regime (Fig. taken from Breitschwerdt & de Avillez 2007).

1965) does not take into account the turbulent nature of the flow. Gas can reside in thermally unstable regions if the eddy turnover timescale is less than the cooling time scale.

Since the former depends on the eddy size, we expect a critical wavelength λ_c below which the gas has not enough time to cool down completely. This can be estimated as follows:

$$\tau_{\text{eddy}} \sim \frac{\lambda}{\Delta u} \sim \left(\frac{\rho}{\epsilon}\right)^{1/3} \lambda^{2/3} < \frac{k_B T}{n \Lambda(T)} \quad (2)$$

$$\Rightarrow \lambda < \left(\frac{k_B \bar{m}}{\Lambda_0}\right)^{3/2} \frac{\epsilon^{1/2}}{\rho^2} T^{3/4}, \quad \Lambda(T) = \Lambda_0 T^{1/2} \quad (3)$$

in case of incompressible flow, with k_B , Δu , ϵ , $\Lambda(T)$ being Boltzmann's constant, the velocity fluctuation, the energy input rate per unit mass, and the WNM cooling function, respectively. Using the compressible turbulence model by Fleck (1996) this generalizes to

$$\lambda < \left[\frac{3}{2} \left(\frac{\epsilon_V}{\rho_0^4}\right)^{1/3} \frac{\bar{m} k_B T^{1/2}}{\Lambda_0} l_0^{-4\alpha} \right]^{3/(2-12\alpha)}, \quad (4)$$

where ϵ_V , l_0 and α are the energy input rate per unit volume, the integral scale, and the compressibility of the flow, respectively. For $\alpha \rightarrow 0$, Eq. (3) is recovered. Using typical WNM values of $\epsilon = 10^{-26}$ erg cm $^{-3}$ s $^{-1}$, $n = 0.3$ cm $^{-3}$, $T = 1000$ K and $\Lambda_0 = 1.9 \times 10^{-27}$ erg cm 3 s $^{-1}$ K $^{-1/2}$, we find gas to exist in this temperature regime, if $\lambda < \lambda_c = 3 \times 10^{19}$ cm, in agreement with our simulations (s. Fig. 6).

3.5 Comparison to observations: O VI and electron density distribution

Historically, the ubiquitous O VI absorption line revealed the existence of the hot ISM. Hence its column density distribution is a test case for any viable ISM model. We have used data cubes (de Avillez & Breitschwerdt 2005b), which were calculated prior to the publication of N(O VI) column densities by Oegerle et al. (2005) and Savage & Lehner (2006) and have derived the O VI column densities. For small distances (see the large variations in Fig. 7, left, for $d < 100$ pc), N(O VI) depends on the vantage point, and only for larger distances do the column densities converge. For example inside an evolved bubble, like our Local Bubble, in which turbulent mixing layers exist (Fig. 7, right, zoom-in region), the N(O VI) is higher than in the ‘‘average’’ ISM; this effect is also seen in the FUSE observations. The averaged O VI ion density we found is $\sim 1.8 \times 10^{-8}$ cm $^{-3}$ in agreement with observations. A major difference between heat conduction and turbulent mixing is that the former can only be efficient in regions where strong temperature gradients exist (e.g. at interfaces like contact discontinuities), while turbulence in the ISM depends on SF and hence is ubiquitous in the Galactic disk.

Another ISM plasma characteristic is the distribution of electrons in the WNM and WIM, which can be inferred from pulsar dispersion measures (DM). Such DMs towards 34 pulsars with known parallaxes have been determined by Berkhuijsen & Fletcher (2008), who found that $\log n_e$ follows a Gaussian distribution centered at $10^{-1.83}$ cm $^{-3}$ with a dispersion of $\sigma = 0.22 \pm 0.02$. In NEI, both the number of electrons and their distribution should be different from CIE. Therefore we have performed 3D NEI high resolution simulations, and integrated the electron density along the l.o.s. In addition, for detailed comparison, we have reassessed pulsar dispersion measures up to 8 kpc from the Sun, and $|z| < 200$ pc from the Galactic plane. We find remarkable agreement between the observations and simulations (de Avillez et al. 2012). The distribution follows a lognormal centred at $\mu = 1.4$ with dispersion $\sigma = 0.21$, hence the average electron is 0.04 ± 0.01 cm $^{-3}$. Comparing the left and right panels of Fig. 8, it follows that the electron density is not uniform, but rather clumpy. A large contribution to the electron density in the ISM comes from electrons locked in thermally unstable regimes. A smaller fraction is found in cold regions, in which the electrons are generated due to charge exchange reactions (ionization of H by He recombination), which becomes larger with increasing density. The highest electron concentration by mass is found in the thermally unstable regime with $200 < T < 10^{3.9}$ K. We could further show that, depending on the vantage point in the disk, the minimum and maximum electron column densities along different l.o.s. encompass the observed pulsar DMs. In order to integrate the electron density along such long distances, we have exploited the periodic boundary conditions at the vertical interfaces of our computational box, and continued the l.o.s. accordingly. The lognormal distribution

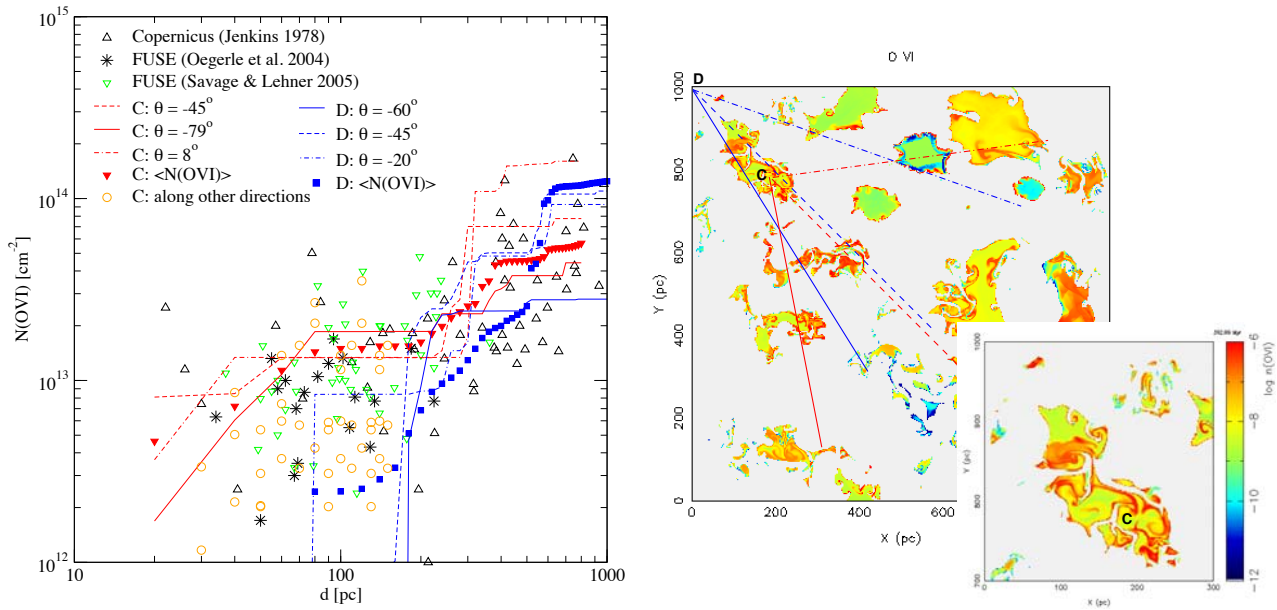


Fig. 7 Left panel: comparison between 3D high resolution numerical simulations of spatially averaged (red triangles and blue squares) and single lines of sight (red and blue lines) of $N(\text{O VI})$ measurements in the simulated disk at time $t = 393$ Myr with observations by FUSE (asterisks: Oegerle et al. 2005; green triangles: Savage & Lehner 2005) and COPERNICUS (black triangles). The LOS are taken at positions C (red) and D (blue), which are located inside and outside of a bubble cavity, respectively, as shown in the right panel. Also shown is the O VI column density in the bubble at position C (orange circles) along other directions than those shown by the red and blue lines. Note that the dispersion in $N(\text{O VI})$ inside the bubble is similar to that observed with FUSE for LOS < 150 pc. Right panel: O VI density distribution (in logarithmic scale) in the midplane at the same time, including a blow-up of the bubble located in position C. Figure is taken from de Avillez & Breitschwerdt (2005b) and reproduced by permission of the AAS.

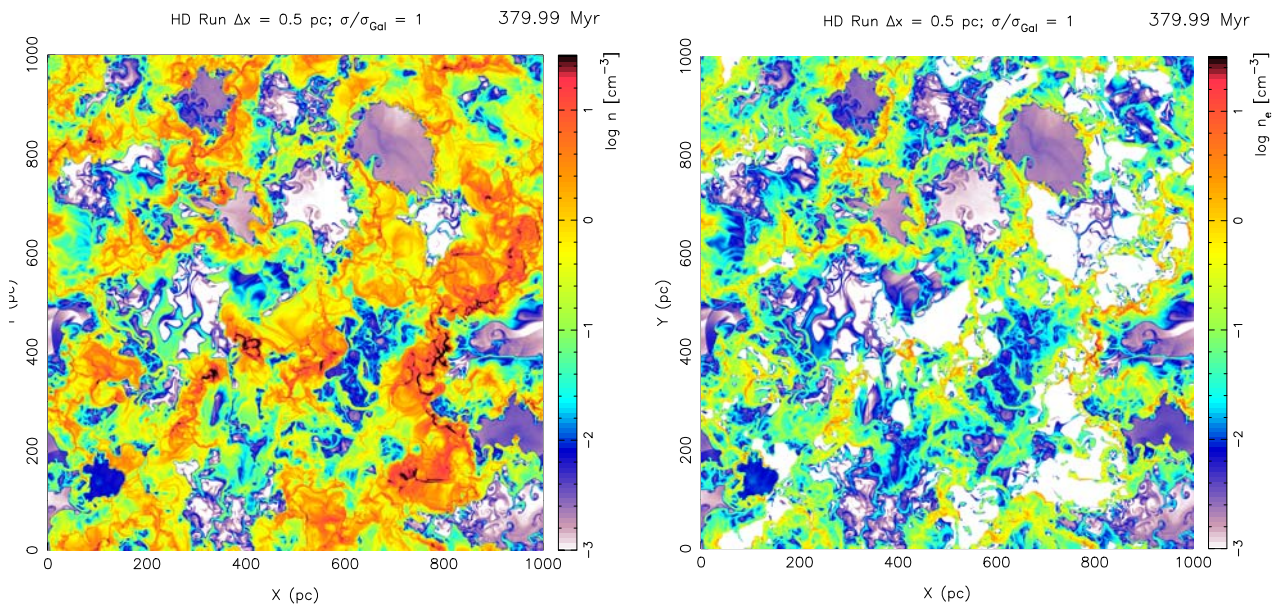


Fig. 8 Logarithmic total (left) and electron (right) density distribution in a Galactic midplane cut (0.5 pc resolution) at 380 Myr of ISM evolution. The red colour coding represents high density gas, with molecular clouds in black. Electron densities smaller than the threshold value of $\log n_e = -4$ (white regions) can be found in both high (atomic and molecular clouds) and lower (bubbles) density regions.

can be understood in terms of the maximum entropy principle. A fully developed turbulent medium has the property of forgetting its initial conditions and can be regarded as a large set of independent random variables. Hence a priori knowledge in the sense of Bayesian statistics is minimized. It can be shown that the Gaussian distribution has the largest entropy among all random variables with equal variance.

4 An ISM test laboratory: the local bubble

Ever since its discovery (s. Sect. 1) the origin of the LB has been a mystery. Early facts were the existence of a HI deficient hole (Local Cavity) and a local X-ray emitting gas (LB), which were anti-correlated on large angular scales. Hence, the so-called “displacement model” (Sanders et al. 1977; Snowden et al. 1991) asserted that the hot plasma pushed away the neutral gas. Shadowing experiments, in which a dense absorber (molecular cloud) at known distance allows to separate foreground from background emission, enable us to determine the emission measure and hence the electron density in the foreground. Assuming a uniformly filled bubble at constant density and temperature, it was thus possible to derive the bubble extension from the emission measure in different directions. It turned out, that the cavity and the LB were not the same in all directions, so that the LB might contain some warm rather than hot gas, and/or is inhomogeneous. In addition, the so-called Long Term Enhancements seen in the ROSAT soft X-Ray spectra argued for the presence of a very local contribution. Analyzing the ROSAT 1/4 keV band emission, Kontroumpa et al. (2009) argue that much of the low latitude emission is due solar wind charge exchange reactions (SWCX) between heavy solar wind ions and interstellar neutrals, streaming into the heliosphere. However, at higher latitude the SWCX effect is too small to account for all of the soft X-ray emission. At present, a combination of both SWCX and more distant hot local bubble plasma seems likely. Both the cavity and the high latitude gas should therefore be due to local SN explosions (e.g. Cox & Smith 2001).

But where are the young massive stars in the solar neighbourhood, survivors of a cluster whose more massive members have created the LB? Since no such cluster is known, we have searched for a moving group that has passed the vicinity of the solar system (Berghöfer & Breitschwerdt 2002), known as the Pleiades subgroup B1; its present day stars are members of the Sco Cen association (see Maiz-Apellaniz 2001). In order to be sure of not having missed other stars, which were not members of the subgroup, Fuchs et al. (2006) searched the complete volume of 400 pc in diameter, centred at the solar system, in the Hipparcos catalogue, combined with the ARIVEL catalogue for space velocities. By selecting only the blue stars, which were concentrated in real and velocity space, we were able to calculate backwards the trajectories of a group of 79 stars, which are the survivors of a moving group. Using an initial mass function (IMF), it is possible to infer the number of

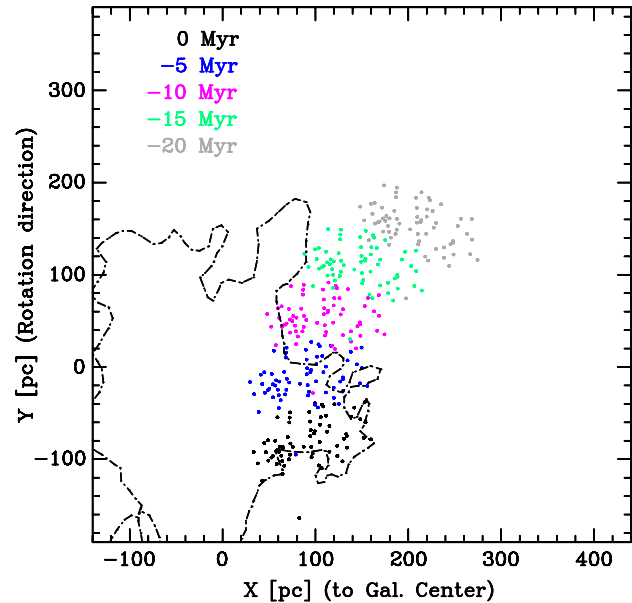


Fig. 9 Path of our moving group stars over the last 20 Myrs projected onto the Galactic plane at different times (colour coded). The observed contour of the LB is dash-dotted.

SN explosions in the past (mass binning was done in such a way that in each integer mass bin there was at least one star), determine their explosion sites from the trajectory and their explosion times from their main sequence life time, assuming that all stars in the cluster were born coevally. The cluster age was determined by putting the clusters stars (after careful de-reddening) into a colour-magnitude diagram, and determining with the help of isochrones (Schaller 1992) their turn-off point.

We find that the age of the LB is about 14 Myr, with ~ 16 explosions having taken place. Figure 9 shows that the cluster path was close to the edge of the LB. The reason that the LB expansion was rather in the anti-centre direction is because of its interaction with the adjacent Loop I superbubble (Egger & Aschenbach 1995), which was generated by explosions in a *different* subgroup of the Sco Cen association, almost at the same time. These studies give us the unique opportunity to find out when and where the closest to Earth recent SN explosion took place, since we know the trajectory and the mass distribution of stars. Some time ago, Knie et al. (2004) have measured the ^{60}Fe content in the ferromanganese crust of the ocean floor, and have found a peak at 2.8 Myr ago, which shifted to 2.2 Myr applying the newly measured ^{10}Be half-life (Feige et al. 2012, <http://www.publish.csiro.au/paper/AS11070.htm>) for dating. Since ^{60}Fe is generated by s-process in massive stars, we can take ^{60}Fe yields as a function of their mass from stellar evolution calculations, and may infer its amount at the solar circle, where it is finally deposited on Earth. The distance, found from SNR expansion calculations, of the closest to Earth SN is thus ~ 85 pc, in excellent agree-

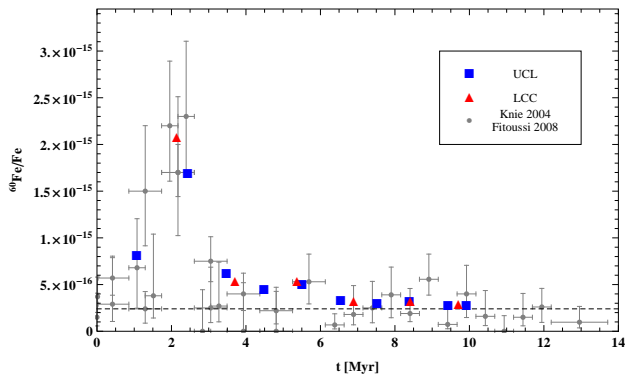


Fig. 10 (online colour at: www.an-journal.org) ^{60}Fe data (with error bars) from Knie et al. (2004) and Fitoussi et al. (2008), and the yields calculated from nearby SNe transported to Earth by shock waves. SNe belonged to the still existing subgroups Upper Centaurus Lupus (UCL) and Lower Centaurus Crux (LCC).

ment (s. Fig. 10) with the measured ^{60}Fe values. This will be described in more detail in forthcoming papers.

5 Conclusions

Despite its long history the ISM is a very active area of astrophysics, and still offers lots of surprises to the researcher. Recent technological advances, both theoretically and observationally, have given an immense thrust to the field. 3D high resolution numerical simulations allow to follow the system far into the nonlinear regime, so that turbulence can be fully developed and a “multiphase” medium is generated. In the results presented here, the turbulent driver were SN explosions, which dominate the energy input. The model can be made self-consistent by closing the feedback loop via SF, according to an IMF in Jeans unstable regions. From the integral scale, where turbulence is fed in, down to the Kolmogorov microscale, where the energy is dissipated, the scale covers too many orders of magnitude to be resolved even with the most powerful computers. Without a realistic subgrid model to bridge the gap, most simulations use numerical instead of viscous dissipation. But there is a caveat, because there is no guarantee that the turbulent spectrum will not be changed. Many ISM studies use therefore artificial forcing, which is a mixture between solenoidal and dilatational energy input rate. This, however, ignores that turbulence is characterized by a large number of degrees of freedom, which cannot be captured by a simple driver. Also the generation of turbulence by tapping the mean flow is highly time-dependent, so that forcing can at best be used for testing processes in modeling. These problems show that in spite of the progress we have made so far, there is still a long way to go, presumably leaving numerical simulations for a long time to be the best tool to study the ISM.

Acknowledgements. DB thanks the organizers for their invitation and financial support. M.A. acknowledges the financial support by the Foundation for Science and Technology (FCT; Portugal) through projects POCTI/FIS/58352/2004, PTDC/FIS/70878/2006, and PTDC/CTE-AST/70877/2006. Most of the simulations described here have been carried out at the Milipeia Supercomputer (Center for Computational Physics, University of Coimbra) and at the ISM-Cluster of the Computational Astrophysics Group (Dept. of Mathematics, University of Évora).

References

- Berkhuijsen, E.M., Fletcher, A.: 2008, *MNRAS* 390, L19
 Berghöfer, T., Breitschwerdt, D.: 2002, *A&A* 390, 299
 Bower, C.S., Field, G.B., Mack, J.E.: 1968, *Nature* 217, 3
 Breitschwerdt, D., de Avillez, M.A.: 2007, in: B.G. Elmegreen, J. Palous (eds.), *Triggered star formation in a turbulent ISM*, p. 57
 Breitschwerdt, D., Schmutzler, T.: 1994, *Nature*, 371, 774
 Breitschwerdt, D., Schmutzler, T.: 1999, *A&A* 347, 650
 Cappellaro, E., Evans, R., Turatto, M.: 1999, *A&A* 351, 459
 Cox, D.P., Anderson, P.R.: 1982, *ApJ* 253, 268
 de Avillez, M.A., Breitschwerdt, D.: 2004, *A&A* 425, 899 (AB04)
 de Avillez, M.A., Breitschwerdt, D.: 2005a, *A&A* 436, 585 (AB05)
 de Avillez, M.A., Breitschwerdt, D.: 2005b, *ApJ* 634, L65
 de Avillez, M.A., Breitschwerdt, D.: 2007, *ApJ* 665, L35
 de Avillez, M.A., Breitschwerdt, D.: 2012a, *A&A* 539, L1 (AB12a)
 de Avillez, M.A., Breitschwerdt, D.: 2012b, in prep.
 de Avillez, M.A.: 2000, *MNRAS* 315, 479
 de Avillez, M.A., Ashgekar, A., Breitschwerdt, D., Spitoni, E.: 2012, *MNRAS*, in press, astro-ph/1204.1511
 Egger, R., Aschenbach, B.: 1995, *A&A* 294, L25
 Elmegreen, B.G., Scalo, J.: 2004, *ARA&A* 42, 211
 Ferrière, K.: 2001, *Rev. Mod. Phys.* 73, 1031
 Field, G.B.: 1965, *ApJ* 142, 531
 Field, G.B., Goldsmith, D.W., Habing, H.J.: 1969, *ApJ* 155, L149
 Fitoussi, C., et al.: *Phys. Rev. Lett.* 101, 121101
 Fleck, R.C., Jr.: 1996, *ApJ* 458, 739
 Freeman, K.C.: 1987, *ARA&A* 25, 603
 Fuchs, B., Breitschwerdt, D., de Avillez, M.A., Dettbarn, C., Flynn, C.: 2006, *MNRAS* 373, 993
 Gressel, O., Elstner, D., Ziegler, U., Rüdiger, G.: 2008, *A&A* 486, L35
 Hartmann, J.: 1904, *ApJ* 19, 268
 Heiles, C., Troland, T.H.: 2003, *ApJ* 586, 1067
 Jenkins, E.B., Meloy, D.A.: 1974, *ApJ* 193, L121
 Kafatos, M.: 1973, *ApJ* 182, 433
 Knie, K., et al.: 2004, *Phys. Rev. Lett.* 93, 171103-1
 Kolmogorov, A.N.: 1941, *Akad. Nauk SSSR Dokl.* 30, 299 (K41)
 Koutroumpa, D., Lallement, R., Raymond, J.C., Kharchenko, V.: 2009, *ApJ* 696, 1517
 Korpi M. J., et al.: 1999, *ApJ* 514, L99
 Kritsuk, A.G., Norman, M.L., Padoan, P., Wagner, R.: 2007, *ApJ* 665, 416
 Kulsrud, R.M., Pearce, W.D.: 1969, *ApJ* 156, 445
 Maiz-Apellaniz, J.: 2001, *ApJ* 560, L83
 Mac Low, M.-M., Klessen, R.S.: 2004, *Rev. Mod. Phys.* 76, 125
 McCammon, D., Sanders, W.T.: 1990, *ARA&A* 28, 657
 McKee, C.F., Ostriker, J.P.: 1977, *ApJ* 218, 148
 Meixner, M., et al.: 2006, *AJ* 132, 2268
 Norman, C.A., Ikeuchi, S.: 1989, *ApJ* 345, 372

- Oegerle, W.R., et al.: 2005, ApJ 622, 3770
Price, D.J., Federrath, C.: 2010, MNRAS 406, 1659
Robitaille, T.P., Whitney, B.A.: 2010, ApJ 710, L11
Rosen, A., Bregman, J. N.: 1995, ApJ 440, 634
Sanders, W.T., Kraushaar, W.L., Nousek, J.A., Fried, P.M.: 1977, ApJ 217, L87
Savage, B.D., Lehnert, N.: 2006, ApJS 162, 134
- Shapiro, P.R., Moore, R.T.: 1976, ApJ 207, 460
Schaller, G., Schaerer, D., Meynet, G., Maeder, A.: 1992, A&AS 96, 269
Smith, R.K., Cox, D.P.: 2001, ApJS 134, 283
Snowden, S.L., et al.: 1991, Sci 252, 1529
von Weizsäcker, C.F.: 1951, ApJ 114, 165